ELSEVIER SAUNDERS

POSITRON EMISSION TOMOGRAPHY

PET Clin 2 (2007) 235–249

Partial Volume Correction Strategies in PET

Olivier Rousset, PhD[a,*], Arman Rahmim, PhD[a], Abass Alavi, MD[b], Habib Zaidi, PhD, PD[c]

In PET imaging, the resolution obtained in the reconstructed images is limited by a combination of various physical and instrumentation-related factors, namely (1) positron range, (2) photon noncollinearity, (3) crystal size and decoding of interacting crystals, (4) the acquisition mode (eg, two-dimensional versus three-dimensional) and the reconstruction algorithm and associated filtering [1]. Because of the limited resolution, the sizes of voxels used in functional imaging are set to be larger than those used in higher-resolution structural modalities such as MR imaging or CT, to avoid excessive noise or sampling artifacts. (In two-dimensional imaging, the term "pixel" is used, but this text assumes the use of three-dimensional imaging, the more usual case.) Therefore an existing problem is the tissue-fraction effect, in which contributions from different tissues, with possibly different tracer uptake and metabolism, may be combined within a single voxel. This problem is not specific to functional imaging but also is of concern in higher-resolution structural imaging modalities such as CT [2] and MR imaging [3]. This effect often is stated as scanner blurring, or point spread, an effect in which activities within a region spill to nearby regions. Both effects originate from the finite resolution capabilities in PET imaging and in reality are two faces of a single

This work was supported by Grant No. SNSF 3100A0-116547 from the Swiss National Foundation, and by Grants RO1AA12839 (NIAAA), K24DA00412-01A1 (NIDA), NS38927 (NIH), and P01HD24448-10 (NIH).

[a] Division of Nuclear Medicine, Russell H. Morgan Department of Radiology and Radiological Sciences, Johns Hopkins University, Johns Hopkins Outpatient Centre, Room 3245, 601 N. Caroline St., Baltimore, MD 21287, USA

[b] Division of Nuclear Medicine, Department of Radiology, Hospital of the University of Pennsylvania, 3400 Spruce Street, Philadelphia, PA 19104, USA

[c] Division of Nuclear Medicine, Geneva University Hospital, CH-1211 Geneva, Switzerland

* Corresponding author.

E-mail address: olivier@jhu.edu (O. Rousset).

1556-8598/07/$ – see front matter

doi:10.1016/j.cpet.2007.10.005

pet.theclinics.com

phenomenon. This unified aspect of partial volume effects (PVE) is reflected in the authors' system of notations, listed in Table 1.

The following discussion assumes a perfectly registered high-resolution image (eg, MR imaging) of the object and a lower-resolution PET image of that same object. The partial volume operator P is denoted as the $n \times m$ matrix modeling the combined tissue-fraction effect as well as the PET point-spread blurring effect (n is the number of PET image voxels, m the number of high-resolution voxels) from the space of the high-resolution image to the PET image space. This notation/model is somewhat different from the common notation in which the tissue-fraction effect is modeled before the point-spread effect and P then is taken as a square matrix modeling the blurring effect on the PET image. In fact, to compute the overall PVE, it is more accurate to perform forward projection of the high-resolution image of the object while incorporating the various finite-resolution effects in PET, followed by application of the reconstruction algorithm used, thus determining the overall PVE (Table 1).

Table 1: **Notations**

Symbol	Definition
b	vector of observed PET image voxels
s	# of tissue segments
x	vector of segment values
m	# of high-resolution (MR imaging) voxels
R	segment to MR imaging mapping
n	# of PET voxels
P	MR imaging to PET partial volume operator
η	voxel noise in PET image
A	region averaging operator
ρ	PET image voxel covariance matrix
B	vector of measured PET region values
G	Geometric Transfer Matrix (GTM)
η'	PET region noise
ρ'	PET region covariance matrix
y	vector of partial volume–corrected image voxels

For many reasons, the first medical applications of positron radiation focused on the brain, and most of the first human PET prototypes were developed specifically for functional brain imaging [4]. Likewise, the first partial volume correction (PVC) techniques focused on neurologic PET procedures in which the enhancement of the quantitative capabilities of PET was driven by brain research [5,6]. The most sophisticated PVC strategies rely on an adjunct coregistered structural image in which MR imaging plays a pivotal role because of the better contrast between the gray and white matter compared with CT [7–10]. Now, however, the use of correlated anatomic information provided by the CT component of dual-modality imaging systems (eg, PET/CT) makes it possible to perform accurate PVC in other organs and tissues including cardiovascular [11], atherosclerotic [12], and whole-body oncologic imaging [13,14].

PVC methods can be categorized broadly as (1) postreconstruction-based and (2) reconstruction-based methods; which are discussed separately in later sections. Within each of these categories, region-of-interest (ROI)–based and voxel-based approaches are discussed. Clinical and research applications of various PVC strategies used in PET are addressed also.

Postreconstruction-based partial volume correction methods

Postreconstruction region-of-interest–based partial volume correction methods

Recovery coefficient method

The first attempts to compensate for PVE using recovery coefficients were made by Hoffman and colleagues [5], who computed a set of recovery coefficients based on known size, shape, and location (within the PET scanner) of the objects being imaged. The same group later extended this approach to predict the recovery coefficients for different brain structures that were approximated using a series of non-overlapping spheres [6]. At this time, the PVE was tackled in the context of hot objects against a cold background and thus dealt with only one aspect of the problem, referred to as "spill-out" (the loss of activity because of the small size of the object relative to the PET scanner's spatial resolution). It soon was realized that, depending on the background's activity concentration, spill-in from the surrounding warm tissues might be as important as spill-out and should be compensated. The concept of contrast recovery coefficient, introduced by Kessler and colleagues [15], reflects the rate of recovery that lies above the surrounding medium. This quantity is justified only when the background itself is not subject to

PVE and is of known concentration and uniform activity.

For simplicity, several investigators adopted this concept and applied formulations derived by Hoffman and Kessler to clinical data to achieve more accurate assessment of relevant parameters (eg, to correct for brain atrophy) [16]. The technique is used commonly in clinical oncology when a priori information about the tumor (ie, a spherical shape of known size) is available [13,17–20]. The approach is limited, however, by the crude approximations involved, and more sophisticated techniques were sought.

Fleming and colleagues [21] have proposed another simple method to account for the PVE by measuring the total uptake rather than the activity concentration in the ROI using a new index, the specific uptake size index. The technique consists in defining volumes of interest for the structure of interest (eg, striatum), large enough to guarantee the inclusion of all the partial volume counts detected outside the physical volume of the structures. The technique was validated further and proved to be useful for accurate quantification of specific binding ratio in Iodine-123 fluoropropyl-2-ß-carbomethoxy-3-ß-(4-iodophenyl)nortropane single proton emission tomography ([^{123}I]FP-CIT SPECT) brain images [22].

Geometric transfer matrix method

The geometric transfer matrix (GTM) method is based on considering as many ROIs as the number of tissue segments considered in the analysis, resulting in as many equations to be solved as the number of unknown true segment values. RSF_i is the regional spread function of tissue i (ie, the response of the scanner to the activity within each tissue segment, which is assumed to be uniform). RSF_i is computed for each segment i by creating an image U_i of the ith segment with unit activity (the other segments being set to 0), followed by the forward projection (*Fproj*) and reconstruction (*Recon*) steps [23–25]:

$$RSF_i = Recon\left(Fproj\,(U_i)\right) \tag{1}$$

The resulting blurred images then define the *RSF* for each segment within which the activity is assumed to be homogeneous, as shown in Fig. 1. Consideration of the issue of noise is elaborated later.

The next step consists in computing what fraction of each segment i contributes to each ROI_j, as shown in Fig. 2; these contributions define the g_{ij} elements of the GTM, denoted here by G.

Next, referring to the vector containing the unknown true tissue segment values as x (size $s \times 1$ where s is the number of tissue segments within which activity is assumed homogeneous) and the vector containing the average measured values within the ROIs drawn on the PET images as B (size $s \times 1$), one arrives at the model:

$$Gx = B \tag{2}$$

In practice, the matrix G is always invertible. One should note that individual ROIs are drawn to correspond closely to each tissue segment, so that the matrix G has most of its largest values along its diagonals. Therefore, the rows or columns of G are not linear combinations of one another, and G can be seen to be invertible. Solving for the vector of unknown segment values x, one then arrives at:

$$x = G^{-1}B \tag{3}$$

wherein the values for vector B are measured regional activity concentrations, and the matrix G has been estimated.

Perturbation-based geometric transfer matrix method

A refinement to this approach, proposed by Du and colleagues [26], is based on the observation that

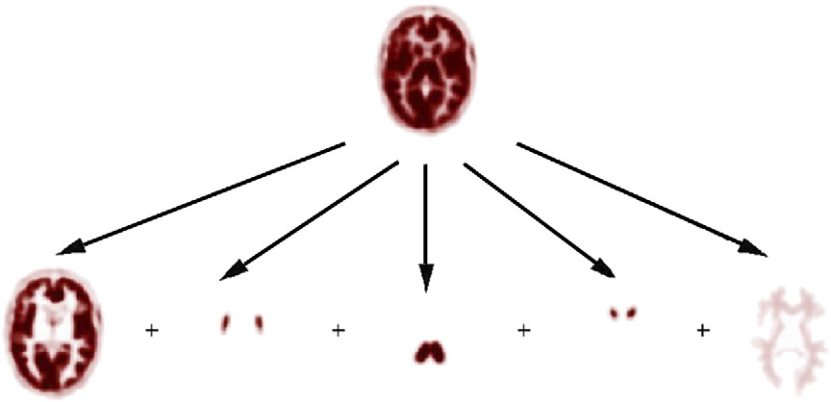

Fig. 1. A PET image is considered as the blurred superposition of tissues of homogeneous activity.

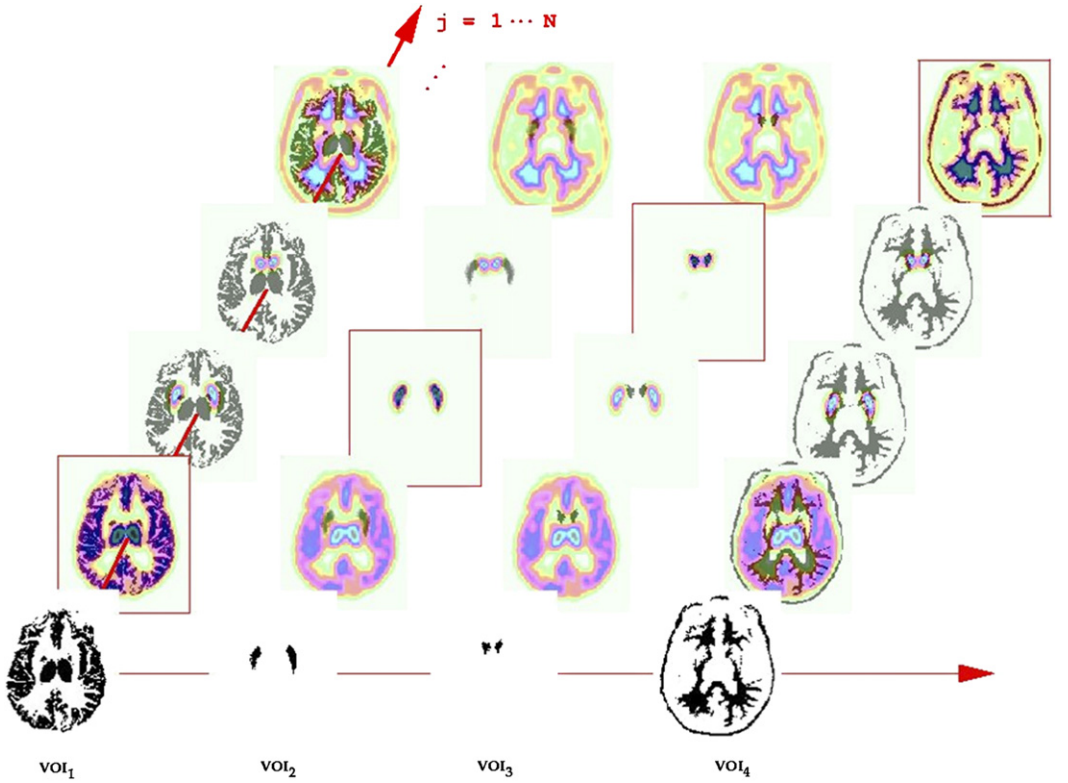

Fig. 2. In this example, four segments of homogeneous activity are assumed: cortical gray matter plus thalamus (VOI_1), putamen (VOI_2), caudate nucleus (VOI_3), and white matter plus scalp (VOI_4). The *RSF* corresponding to each segment is then calculated, and its intersection fraction with each of the ROIs (j = 1…4) is computed, thus defining the elements of the 4 × 4 GTM in this example.

statistical iterative reconstruction algorithms (eg, ordered subset expectation maximization, OSEM) are nonlinear, suggesting that the response of the scanner to a particular segment can depend on the activities in the other segments. The approach proposed by the authors is to perturb the initially estimated image $\tilde{f}$ for the contribution of each segment to arrive at a better estimate of the *RSF* distributions. This approach can be written in our notation as:

$$RSF_i = \frac{1}{d_i}\left\{Recon\left(Fproj\left(\tilde{f}+d_i\,U_i\right)\right) - Recon\left(Fproj\left(\tilde{f}\right)\right)\right\} \quad (4)$$

where d_i is set to be a certain percentage (eg, 10% in Ref. [26]) of the average counts in each segment i. (The notation used by Du and colleagues does not consider the tissue-fraction effect, because it denotes high-resolution segments and PET ROIs in the same space, thus modeling only the point-spread function (PSF) effect. The authors of this article thus extend the notation to the more general case).

The method was tested using phantoms and simulations in the context of brain SPECT imaging and showed noticeable reductions of bias in PVC compared with the conventional method based on the linear assumption [27].

Methods using voxel-based noise models

Alternatives to this approach also have been suggested by Labbe and colleagues [28] and by Aston and colleagues [29]. These alternatives are still ROI based in that they perform PVC for measured ROI values, but they attempt to model the noise at the voxel level. A novel analytic comparison of these methods with the one derived by Rousset and colleagues [25] is presented here.

Approximately following the notations of Aston and colleagues [29], let R be a matrix mapping the true segment values x to the high-resolution (eg, MR) image voxels (thus $m \times s$, where m is the number of high-resolution voxels). As such, elements of R are strictly 0 or 1 for hard segmentation or can take values in the range [0,1] for soft/fuzzy segmentation of MR images. Also, denoting b to

store the reconstructed PET image values at the voxel level (with size $n \times 1$), this model can be written as:

$$PRx + \eta = b \tag{5}$$

where P, as previously defined, maps the MR image to the PET image incorporating the overall PVE (ie, tissue fraction as well as the PSF effect), and η models the noise in the reconstructed PET image that can be generalized to model the contribution of different types of noise. In the present framework, the approach of Rousset and colleagues [25] can be derived by considering the $s \times n$ averaging operator A, which essentially considers s regions (ie, as many regions as the original segments) and calculates the average image values within each region; thus:

$$APRx + A\eta = Ab \tag{6}$$

Which, defining $\eta' = A\eta$, $G = APR$ and $B = Ab$, can be written as

$$Gx + \eta' = B \tag{7}$$

Note that B is thus simply the measured average region values, and G (which is a square $s \times s$ matrix) models the PVE on the original segments as measured by the defined regions and is thus the standard GTM.

Now modeling the noise vector η' using a general region noise covariance matrix ρ' (size $s \times s$), the weighted least-squares solution to Equation 7 (ie, weighted by ρ'^{-1}) is:

$$x = (G^T \rho'^{-1} G)^{-1} G^T \rho'^{-1} B \tag{8}$$

Next, recalling as explained before, that the GTM G is in practice always invertible, one arrives at many cancellations in Equation 8 resulting in:

$$x = G^{-1} B \tag{9}$$

That is, according to this method, the PVC segment values are independent of the noise properties. This important observation shows that the present framework is not biased in the sense that it does not make any assumptions or approximations about the noise distribution in the reconstructed PET images. It also suggests that, in ongoing advanced PVC research, this framework should be used for benchmark comparisons because it makes a minimal number of assumptions. Aston and colleagues [29] are able to reduce their derivation to that of Rousset and colleagues [25] by making an assumption regarding the noise model, but it is not necessary to make that assumption to arrive at the GTM approach. In fact, as argued previously, given the ROI-averaging framework set by Equation 6, one may arrive at Rousset and colleagues' [25] formulation without making specific assumptions about the noise model.

The approach instead can be implemented by directly solving Equation 5, as described by Aston and colleagues [29], at the voxel level. Thus, modeling the voxel noise η using a general image voxel covariance matrix ρ (size $n \times n$), the least-squares solution of Equation 5 weighted by ρ^{-1} yields:

$$x = (R^T P^T \rho^{-1} PR)^{-1} R^T P^T \rho^{-1} b \tag{10}$$

Here, unlike the previous solution, a cancellation of terms does not occur, because the matrix PR is a non-square matrix ($n \times x$) mapping the true segment values to blurred PET images and as such is not invertible. Labbe and colleagues [28] proposed the nonweighted least-squares approach (ie, with an assumption of uncorrelated, identically distributed voxel noise, thus $\rho \propto I$) arriving at:

$$x = (R^T P^T PR)^{-1} R^T P^T b \tag{11}$$

Nevertheless, the aforementioned assumption is generally not valid in PET reconstructions, and the voxels tend to reveal unequal variances, especially with iterative reconstructions in which voxel variances are very nonuniform and typically are highly correlated with true voxel intensities [30,31]. As such, a better approximation worthy of further investigation for OSEM-type algorithms is to set:

$$\rho \sim \mathrm{diag}\{b^2\} \tag{12}$$

where b^2 is the vector of squared imaged intensities, which can be arrived at roughly by using approximate noise analysis for iterative algorithms (see Equation 41 in Ref. [30]). Nevertheless, Equation 12 is still a rough approximation, and the variances depend on the object in a more complicated way, as derived extensively by Barrett and colleagues [30] and more precisely by Qi [31]. Furthermore, it is not accurate to assume that image voxels are uncorrelated, and the amount of correlation is highly dependent on a number of factors (eg, the number of iterations of the reconstruction algorithm and whether resolution recovery methods are used [32]).

The authors believe that the accurate modeling of noise using Equation 10 has considerable potential for obtaining more precise (ie, less variant) PVC estimates. At the same time, the task of estimating the covariance matrix ρ is quite intense [31] and would be compounded further in practice because it would be estimated based on the measured data set, which is only a single, noisy projection of the true object [33]. The degree of valid approximations in the estimation of the covariance matrix ρ that would be acceptable for the task of estimating PVC segment values x remains an open question. Therefore it is useful to compare such derivations

with that of Equation 9, which, as was shown, is independent of the noise model.

Postreconstruction voxel-based methods of partial volume correction

Potential advantages of PVE-corrected images, as opposed to PVE-corrected ROI-measured concentrations, include the ability to delineate functional volumes accurately and to improve the tumor-to-background ratio, which could improve considerably the analysis of response-to-therapy studies and diagnostic examinations as well as treatment planning for PET-based radiation therapy. In this context, however, the problem is more complex and has been attempted frequently, based on a number of often strong assumptions and approximations.

Partition-based methods

To perceive the complexity of the problem, one should note that the true segment distribution $f(r)$ at any voxel r being estimated can be written as:

$$f(r) = \sum_{i=1}^{N} x_i U_i(r) \tag{13}$$

assuming N homogeneous segments each with activity x_i. As such, each voxel can have the contributions of up to N segments (thus one equation with N unknowns for each voxel). The strategy in the ROI-based PVC methods was to set up as many ROIs as there are unknown segments, to arrive at estimated concentrations for the ROIs given the knowledge of the *RSFs*. Within the present context of voxel-based PVC, a simple approach has been to set $N = 1$ [34]. This approach aims to compensate for signal dilution in nonactive tissues such as cerebrospinal fluid (CSF). This compensation is important in the case of tissue atrophy to avoid misinterpreting the decrease of metabolism as being caused by the PVE. Setting $N = 1$ in this equation, while applying the partial volume operator to both sides, gives:

$$b(r) = Pf(r) = x_1 PU_1(r) \tag{14}$$

Assuming entirely consistent reconstructions (ie, no noise) and very accurate modeling of the operator P, solving Equation 14 at any non-zero measured PET voxel would yield the value of x_i. Realistically, however, within segment 1 one may instead define $x_1(r)$ and compute it as:

$$x_1(r) = \frac{b(r)}{PU_1(r)} \tag{15}$$

A more realistic approach proposed by Muller-Gartner and colleagues [35] has been to model presence of three distinct regions: (1) gray matter, (2) white matter, and (3) background and CSF activity. (It is worth paying close attention to whether the detected activity in this third region is not simply the result of spillover from adjacent tissue plus noise.) The relevant equation in this case is:

$$b(r) = Pf(r) = x_1 PU_1(r) + x_2 PU_2(r) + x_3 PU_3(r) \tag{16}$$

The approach is based on assuming the presence of ROIs within regions 2 and 3 such that they are not contaminated by PVEs (thus extracting values of x_2 and x_3). Similar to the $N = 1$ case, $x_1(r)$ now can be estimated as:

$$x_1(r) = \frac{b(r) - x_2 PU_2(r) - x_3 PU_3(r)}{PU_1(r)} \tag{17}$$

This approach, for the simplified $N = 2$ case (activity only in gray and white matter) is depicted in Fig. 3.

Another method proposed by Rousset and colleagues [36], and later incorporated in the software described by Quarantelli and colleagues [37], has been to extract the white matter activity using ROI-based PVC methods, followed by application of this calculation. The Muller-Gartner method was extended by Meltzer and colleagues [38] for the case $N = 4$ wherein a voxel of interest with distinct activity (amygdala) is considered within gray matter. The same group also reported on the comparative analysis of two- and three-compartment methods and concluded that the two-compartment approach is better suited for comparative PET studies, whereas the three-compartment approach provides better accuracy for absolute quantitative measures [39].

In comparison with the ROI-based PVC methods, the aforementioned ($N > 1$) approaches are (1) based on the assumption of possibility of extracting non–partial volume–contaminated activities from some remote ROIs (particularly for white matter and CSF), and additionally (2) tend to limit N to a very few regions to provide solutions to the multi-unknown problem. By contrast, the ROI-based methods are based on a collective modeling of the ROIs' partial volume contributions to one another, rather than focusing on individual voxels at each computation. A quantitative comparison of the methods is provided in [36]. Nevertheless, the search for voxel-based PVC remains appealing, and deconvolution methods have seemed natural for this problem, as discussed in the following section.

Iterative deconvolution methods

One intuitive approach to this problem, which does not require the use of a high-resolution modality or assumptions regarding surrounding structures, is to employ analytic deconvolution

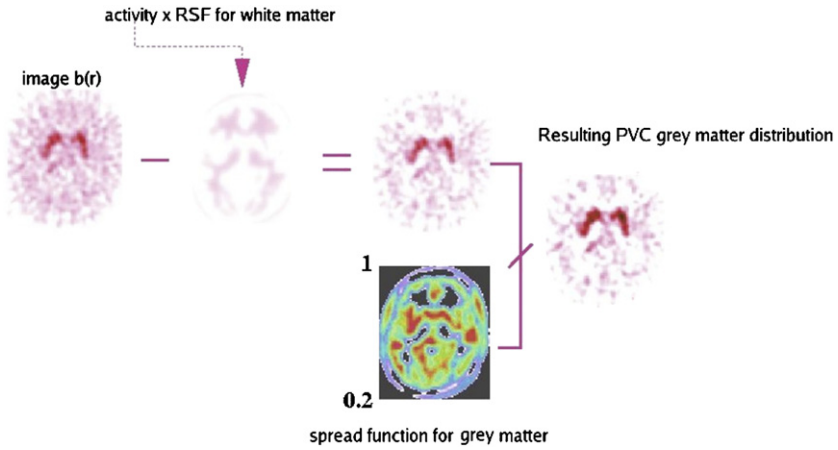

Fig. 3. A simplified depiction of the Muller-Gartner approach for the $N = 2$ case (gray matter, white matter). The term $x_2[activity] \times PU_2[RSF]$ for white matter is subtracted from the original image *b(r)*, followed by division, within the ROI for the gray matter, by its regional spread function, which is typically thresholded (eg, 20%) to avoid amplification of noise.

methods, because the PVE typically is presented as a convolution of the original image with the system PSF (which may well be space-variant). Nevertheless, because of the presence of noise in the images, and because simple deconvolution methods amplify the high-frequency content of images, thus making the resulting images unsuitable for visual interpretation, more advanced approaches are needed. Many alternatives have been described in the literature. (Readers are encouraged to consult Schafer and colleagues [40] and especially Carasso [41].) In the Richardson-Lucy algorithm derived from Bayes's theorem (and not necessarily based on additional noise assumptions, although Poisson's assumption also arrives at same solution), one uses [41]:

$$\gamma^{i+1} = \gamma^i \times P^T \frac{b}{P\gamma^i} \tag{18}$$

where the partial volume–corrected image, vector γ, is iteratively estimated (from iteration i to $i+1$) from the partial volume–contaminated image, vector b, and the estimated blurring matrix, P. The algorithm, however, gives the inverse filtering solution when iterated until convergence [41], thus needing to be terminated early or regularized.

Another notable alternative has been the application of the reblurred VanCittert method [41]:

$$\gamma^{i+1} = \gamma^i + \lambda P^T \left(b - P\gamma^i\right) \tag{19}$$

where $\lambda \in (0, 2)$is a constant that controls convergence. The method can be derived by application of the steepest descent scheme to the minimization of $||P\gamma\text{-}b||^2$ (ie, least-squares criterion based on the Gaussian model). Like the Richardson-Lucy algorithm, however, this method iteratively results in increasingly noisy image estimates, suggesting the need for early termination or use of regularization (eg, see Ref. [42]). For a review of these and alternative methods (eg, the Poisson maximum a priori maximum entropy, Tikhonov-Miller restoration, and linear slow evolution from the continuation boundary [slow evolution from the continuation boundary] methods), the reader is referred to Carasso [41].

One such approach was implemented recently in the context of oncologic PET imaging. The authors used an iterative three-dimensional deconvolution algorithm and a local model of the PET scanner's PSF followed by application of a PVE correction to the mean voxel value within a voxel of interest [43]. The authors report more accurate quantitative assessments of uptake in lesions greater than 1.5 × full-width at half-maximum (FWHM) of the imaging system's PSF.

Multi-resolution approach

A newer approach makes use of the multi-resolution method [44]: the algorithm extracts details of a high-resolution image (eg, MR imaging) and transforms these details to integrate them into a low-resolution image (eg, PET). The method proposes using wavelet analysis to decompose the images into layers of different resolution/frequency content. The high-resolution (eg, MR) image therefore will result in additional levels of resolution images, from which, it is proposed, the details lost in the low-resolution image can be constructed. The study used a purely linear model of scaling the wavelet-transformed

images between the two modalities studied; this linear model does not seem to be justified, except that it results in ROI quantitation comparable with that obtained by standard PVC methods. This method seems to be quite promising and remains to be extended by more accurately relating the transformed resolution levels of high-resolution and low-resolution modalities.

Combined noise and partial volume correction model

Another promising method proposed by Chiverton and colleagues [45] is the use of an elaborate statistical framework for combining image noise reduction and partial volume estimation. The approach works by considering the relationship between true voxel concentrations and the composite (ie, partial volume–contaminated) voxel concentrations, as well as the statistical relations between composite values and the noisy realizations. The latter component, however, is assumed to obey Gaussian statistics, an assumption that may be inadequate, especially for low-statistics data. This distribution can be highly dependent on the type of reconstruction method used [30,31]. This approach still needs to be validated more thoroughly.

Reconstruction-based partial volume correction methods

PVC commonly is presented in the context of compensating for the spill-in/spill-out effects present in reconstruction images, resulting from the limited resolution capabilities of the imaging system. One therefore would think that, for a structure of a given size, the higher the resolution of a modality, the less the PVE will be. Another way of thinking about this problem, however, is to note that improving the resolution of reconstructions performed on a given scanner would, in effect, be a move in the direction of PVC. Reconstruction methods that improve the effective resolution of the scanner (at a given noise level) can be considered as PVC methods. In this sense, there are numerous approaches to reconstruction that attempt to achieve the aforementioned goals [46,47]; the use of statistical iterative reconstructions has been an important step in this direction both for voxel-based [11,48] and ROI-based [49–52] reconstructions. Within the context of these algorithms (and building on them), a number of recent methods deserve to be highlighted.

Voxel-based methods

Resolution recovery methods

In resolution recovery methods, the system matrix is modeled more accurately to incorporate the blurring effects in PET (positron range, noncollinearity, intercrystal scattering and/or crystal penetration effects). A number of such methods exist and have been reviewed elsewhere [53]. These methods have been shown to result in considerably improved contrast-versus-noise plots for extended objects, because of better modeling of blurring effects in PET (ie, higher effective resolution, and thus less PVE, at a given noise level) [54,55].

Bayesian methods

Bayesian methods were developed originally to suppress noise in PET reconstructed images by penalizing voxel variations between neighboring voxels [56]. More sophisticated methods involved the use of anatomic information from MR imaging or CT to avoid blurring effects at the boundaries of regions, as reviewed extensively by Rousset and Zaidi [53]. As such, these methods obtain improved noise levels at nearly similar contrast and effective resolutions. Alternatively, Bayesian methods can be thought of as obtaining improved contrast and effective resolution at a given level of noise, thus reducing the PVE.

The main problem with these methods, however, has been the introduction of bias in the reconstruction images because of strong assumptions of uniformity correlations between anatomic and functional regions. By contrast, Zhang and colleagues [57] and Bowsher and colleagues [58] have proposed elaborate and involved methods that are able to account for exceptions to the assumed anatomy–function correlation and thus allow for the possibility that intensity regions in the emission reconstruction may not correspond to regions in the anatomic image. These methods, however, require some user interactions and the estimation of several hyperparameters. A joint mixture framework proposed by Rangarajan and colleagues [59] offers the aforementioned advantage but does not involve user interactions or the need to determine complicated hyperparameters.

Region-of-interest–based methods

A different, novel approach to this problem has been to quantify ROIs directly from projection data, taking into account the effect of PVE (among other effects, such as scatter). Derived from the early work of Huesman [49], this approach has been developed and investigated by Muzic and colleagues [60] in cardiac imaging, by Chen and colleagues [61] and Schoenahl and Zaidi [62] in tumor imaging, and by Vanzi and colleagues [52] in dopamine transporter imaging. This method has the particular advantage of being able to estimate region variance for subsequent use in model analysis to obtain

parameter estimates; however, these methods remain to be extended to three-dimensional imaging.

Clinical and research applications of partial volume correction

Quantitative PET measurements of physiologic and biologic processes in vivo are influenced by various physical degrading factors including partial volume averaging among neighboring tissues with differing tracer concentrations resulting from the limited spatial resolution of state-of-the-art PET scanners. PVC is important for describing the true functional contribution of PET in providing clinicians and scientists with relevant functional information in various pathologies. This information might allow accurate quantification of physiologic processes including cerebral blood flow, glucose metabolism, neuroreceptor binding, tumor metabolism, and myocardial perfusion.

It has been shown in brain PET imaging that, despite substantial improvements in PET scanners' spatial resolution, the loss of cerebral volume resulting from healthy aging processes can cause underestimation of PET physiologic measurements. Thus, the failure to account for the effect of partial volume averaging of brains with expanded sulci has contributed to the confounding results in functional imaging studies of aging. After PVC, no cerebral blood flow decline with age in healthy individuals is described [63–65]. Likewise, it has been demonstrated that reduced glucose metabolism measured by PET in dementia of the Alzheimer type is not simply an artifact caused by an increase in CSF space induced by atrophy but reflects a true metabolic reduction per gram of tissue [66]. In epileptic foci, also, hypometabolism is larger than a mere atrophy effect [67]. Assessment of the dopaminergic system with PET has shown that dopamine transporters are noticeably reduced in Lesh-Nyhan disease; PVC highlights this finding [68]. Dopa-decarboxylase activity has been shown to be reduced greatly in patients who have Parkinson disease, compared with normal controls [69].

In myocardial imaging, the use of recovery coefficients and spillover factors derived either theoretically or using experimental measurements was popular in the 1980s [70,71]. The same approach was used for the quantification of myocardial blood flow using Nitrogen-13–labeled (^{13}NH3) ammonia [72] where the spillover from the blood pool into the myocardial wall was significant. Partial volume losses in the myocardium also can be estimated using an extravascular density image, created by the subtraction of a blood pool from a transmission image [73]. The authors have shown that the extravascular density image can correct for partial volume averaging over a range of myocardial thicknesses applicable to patient studies. Nevertheless, the method was found to be sensitive to errors in both the blood pool and transmission images in the thinnest regions.

A more appealing approach taking advantage of the availability of correlated structural imaging (CT) was proposed to derive count recovery maps in SPECT myocardial perfusion imaging that was validated experimentally in an elegant study using a porcine heart model [11]. This method could be extended easily for use in cardiovascular PET imaging but would be challenging to apply in tumor imaging because of the difficulties in delineating accurately the metabolically active parts of a tumor (eg, in lesions with wholly or partially necrotic centers) using structural imaging [14].

In tumor imaging, several studies reported that PVE is a serious issue that affects both image quality and the quantitative accuracy of estimated indices characterizing lesion uptake, such as the standardized uptake value (SUV). The most straightforward approach uses a set of precalculated recovery coefficients for more reliable estimates of the SUV in pulmonary lesions [20,74,75] and breast cancer [76]. The bias affecting estimates of tumor-to-background ratio resulting from the PVE is dependent on lesion size. The generally accepted criterion is that PVC is required if the lesion size is less than two to three times the spatial resolution (FWHM) of the imaging system when the parameter of interest is the maximum voxel value within a particular voxel of interest. In fact, it has been demonstrated that when the parameter of interest is the average count density, the bias introduced by the PVE could exceed 10%, even for lesions 0 ~ 6 times the FWHM, depending on the true tumor-to-background ratio [77].

As mentioned previously for cardiac imaging, the lesion size determined by structural imaging (CT or MR imaging) also can be used to compensate for PVE, thus allowing a more accurate estimate of the SUV. Hickeson and colleagues [13] reported an increase in accuracy from 58% to 89% by using this technique for assessing the metabolic activity of lung nodules measuring less than 2 cm when a SUV threshold of 2.5 was adopted to distinguish between benign and malignant lesions (Fig. 4). Similar techniques also were used for preclinical imaging using a clinical PET/CT scanner. High-resolution CT is used for more precise localization of PET findings in addition to PVC through size-dependent recovery coefficient correction [78].

The use of global metabolic activity (obtained by multiplying segmented MR imaging volumes by the measured mean cerebral metabolic rates for glucose

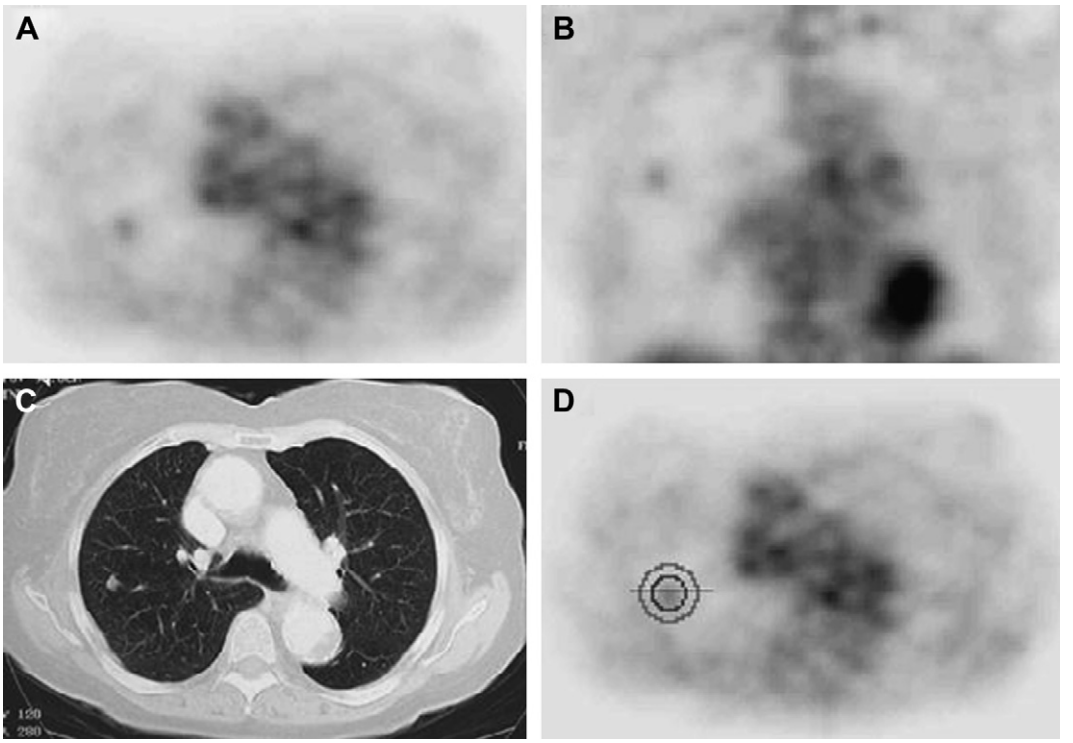

Fig. 4. Images of a 72-year-old woman with small cell lung carcinoma. (*A*) Transaxial and (*B*) coronal images of FDG-PET scan demonstrate focus of mildly increased uptake in right middle lobe. The maximum standardized uptake value (SUV_{max}) was 1.39, which is less than threshold for malignancy. (*C*) Transaxial chest CT image demonstrates that nodule measures 1.0 × 0.8 cm. Corrected SUV was obtained by drawing ellipsoid or circular ROI (in black) with diameter of 0.8 cm (two voxels) larger than that of the area of perceived increase in activity at plane of maximal FDG uptake, and drawing another ROI (in gray) with diameter of 0.8 cm larger than first ROI to determine background activity (activity per volume outside smaller ROI and inside larger ROI). Corrected SUV then was obtained by determining activity in first smaller ROI corrected for background activity, dividing by lesion's size on CT and ratio of injected dose to body mass, and correcting for decay of ^{18}F. Corrected SUV of this lesion was 3.54, which exceeds threshold for malignancy. (*From* Hickeson M, Yun M, Matthies A, et al. Use of a corrected standardized uptake value based on the lesion size on CT permits accurate characterization of lung nodules on FDG-PET. Eur J Nucl Med Mol Imaging 2002;29:1639–47; with kind permission from Springer Science and Business Media.)

using PET), introduced by Alavi and colleagues [10] in assessment of the brain in patients who had Alzheimer disease and in age-matched controls, has made possible the accurate measurement of the global metabolic activity of the red marrow using segmented MR imaging for PVC of PET data [79]. This strategy may have potential research and clinical applications in the study of the global metabolic activity of the individual component and in the diagnosis of benign and malignant bone marrow disorders.

Potential pitfalls

Despite the remarkable advances and achievements to date, PVC still is limited by the inaccuracies of the various procedures involved in the implementation of sophisticated methods, particularly those relying on an adjunct structural modality image (CT or MR imaging). These limitations, which include the spatial realignment of functional and anatomic images, segmentation of the high-resolution anatomic image, and tissue inhomogeneities, are discussed briefly.

Image registration

Dual-modality imaging systems provide a hardware approach to spatial alignment of functional and anatomic images that is of particular value when numeric algorithms fail. Software approaches remain vital to the solution of many registration problems in clinical practice, however, and might even complement hardware approaches in many cases [80]. The accuracy of the PVC techniques will depend in part on the accuracy of the realignment of the anatomic and functional images. The impact of

misalignment has been investigated in the context of brain imaging for the region-based approach [25,37,81,82] and for the pixel-based approaches [35,37,38,83]. For the GTM approach, the errors resulting from misregistration affect only the observed estimates and do not modify the coefficients of the GTM matrix. Therefore, the effect of the registration error on the corrected estimates is of the same magnitude as the effect of misregistration on the observed estimates because of inaccurate placement of the ROIs [82]. It has been shown that these errors have a relatively modest impact on the final accuracy of the corrected estimates (< 2% of true value for typical 1- to 2-mm misregistration errors) [81,82]. Some authors, however, suggested recently that misregistration errors have the strongest impact on data accuracy and precision [37].

Anatomic image segmentation

Medical image segmentation has been identified as the key problem of medical image analysis and remains a popular and challenging area of research [84]. In brain MR imaging, a wide variety of brain MR imaging segmentation techniques, including a number of promising approaches, have been devised and are described in the literature [85]. Similar to image registration, the accuracy of algorithms for PVC depends in part on the degree of accuracy in the segmentation of the anatomic images. Errors in the segmentation procedure have greater impact but are relatively limited to the mis-segmented region [81]. Overall, the accuracy of the corrected estimates seems to be impacted more by the success of the segmentation of the structural information provided by MR imaging than by the influence of image co-registration. Zaidi and colleagues [86] investigated the impact of brain MR image segmentation on PVC. Three algorithms were compared: the first, bundled in the Statistical Parametric Mapping package [87], and the second, the Expectation Maximization Segmentation algorithm [88], incorporate a priori probability images derived from MR images of a large number of subjects. The third, referred to as the "histogram-based segmentation algorithm (HSBA) algorithm," is a histogram-based segmentation algorithm incorporating an Expectation Maximization approach to model a four-Gaussian mixture for both global and local histograms [89]. Fig. 5 illustrates an example in which brains were extracted inappropriately using the brain extraction tool for the HBSA segmentation. Regions where some degree of atrophy was present were extracted as nonbrain matter by the brain extraction tool. It was concluded that the PVC activities in some regions of the brain show large relative differences when performing paired analysis on two algorithms, indicating that the segmentation algorithm for ROI-based PVC must be chosen carefully.

It was suggested that, in the absence of major sources of registration or segmentation errors, recovered activity concentration estimates were typically within 5% to 10% of the true tracer concentration with an SD of a few percent in both phantom and simulation studies [25,29,37,81]. Potential innovative developments for future simultaneous PET/MR imaging technology dedicated for brain research [90] would be combining various MR imaging segmentation methods to compensate for both PVC and attenuation [91].

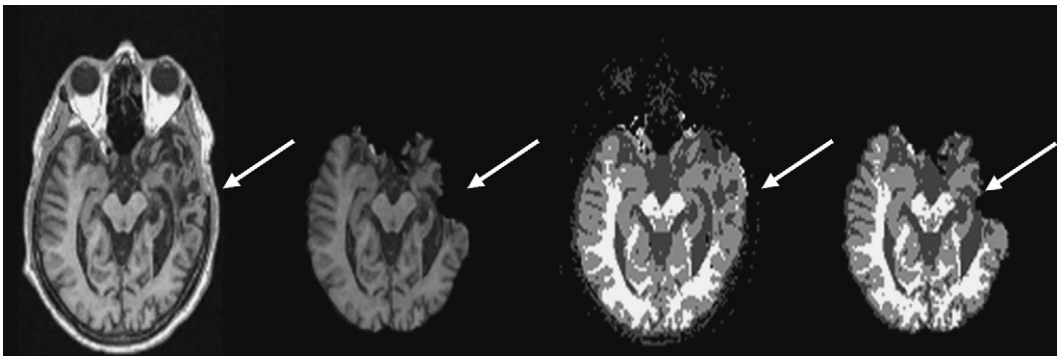

Fig. 5. Representative slices of clinical T1-weighted MR images segmentation. Images from left to right show the patient's original MR images coregistered to corresponding PET image; the segmentation result using the algorithm bundled in the Statistical Parametric Mapping package [87]; the Expectation Maximization Segmentation algorithm [88]; and a histogram-based segmentation algorithm [89]. White areas correspond to white matter, light gray areas to gray matter, and dark gray areas to cerebrospinal fluid. Arrows show discrepancies between segmentation results. Because of brain extraction, atrophic regions were removed. Arrows indicate possible errors.

Tissue inhomogeneity

Inaccuracies resulting from mis-segmentation can be considered in the context of a more general problem of tissue heterogeneity. In fact, the key limiting factor of these techniques is the hypothesis made regarding the homogeneity of tracer distribution in each region or tissue component. Some investigators gave suggested performing tests of inhomogeneity based on Krylov subspace iteration to assess the suitability of assuming a homogeneous tracer distribution [29]. This test, however, is valid only when an accurate noise model is available, which is still a challenging task. If known a priori, the tissue mixture of each identified component can serve as a basis for computing the required *RSFs*. This computation can be performed using statistical probabilistic anatomic maps that can be defined as the probability of each tissue class (eg, gray matter, white matter, CSF) being present in a given location of a standardized, or stereotaxic space [92].

Summary

It is gratifying to see the progress that PVC has made in PET. Recent developments have been enormous, particularly in the last decade. The focus has been on improving accuracy, precision, and computational speed through efficient implementation in conjunction with decreasing the amount of operator interaction. PVC of PET data is well established in research environments, but its use in clinical settings is still limited to institutions with advanced technical support. As the challenges discussed in this article are met, and experience is gained, implementation of validated techniques in commercial software packages will be useful to attract the interest of the clinical community and increase the popularity of these tools.

References

[1] Zaidi H, Alavi A. Current trends in PET and combined (PET/CT and PET/MR) systems design. PET Clinics, in press.
[2] Hsieh J. Nonlinear partial volume artifact correction in helical CT. IEEE Trans Nucl Sci 1999;46: 743–7.
[3] Van Leemput K, Maes F, Vandermeulen D, et al. A unifying framework for partial volume segmentation of brain MR images. IEEE Trans Med Imaging 2003;22:105–19.
[4] Zaidi H, Montandon M-L. The new challenges of brain PET imaging technology. Curr Med Imag Rev 2006;2:3–13.
[5] Hoffman EJ, Huang SC, Phelps ME. Quantitation in positron emission computed tomography: 1. Effect of object size. J Comput Assist Tomogr 1979;3:299–308.
[6] Mazziotta JC, Phelps ME, Plummer D, et al. Quantitation in positron emission computed tomography: 5. Physical-anatomical effects. J Comput Assist Tomogr 1981;5:734–43.
[7] Chawluk JB, Alavi A, Dann R, et al. Positron emission tomography in aging and dementia: effect of cerebral atrophy. J Nucl Med 1987;28:431–7.
[8] Tanna NK, Kohn MI, Horwich DN, et al. Analysis of brain and cerebrospinal fluid volumes with MR imaging: impact on PET data correction for atrophy. Part II. Aging and Alzheimer dementia. Radiology 1991;178:123–30.
[9] Kohn MI, Tanna NK, Herman GT, et al. Analysis of brain and cerebrospinal fluid volumes with MR imaging. Part I. Methods, reliability, and validation. Radiology 1991;178:115–22.
[10] Alavi A, Newberg AB, Souder E, et al. Quantitative analysis of PET and MRI data in normal aging and Alzheimer's disease: atrophy weighted total brain metabolism and absolute whole brain metabolism as reliable discriminators. J Nucl Med 1993;34:1681–7.
[11] Da Silva AJ, Tang HR, Wong KH, et al. Absolute quantification of regional myocardial uptake of 99mTc-sestamibi with SPECT: experimental validation in a porcine model. J Nucl Med 2001; 42:772–9.
[12] Bural GG, Torigian DA, Chamroonrat W, et al. Quantitative assessment of the atherosclerotic burden of the aorta by combined FDG-PET and CT image analysis: a new concept. Nucl Med Biol 2006;33:1037–43.
[13] Hickeson M, Yun M, Matthies A, et al. Use of a corrected standardized uptake value based on the lesion size on CT permits accurate characterization of lung nodules on FDG-PET. Eur J Nucl Med Mol Imaging 2002;29: 1639–47.
[14] Soret M, Bacharach SL, Buvat I. Partial-volume effect in PET tumor imaging. J Nucl Med 2007; 48:932–45.
[15] Kessler RM, Ellis JR, Eden M. Analysis of emission tomographic scan data: limitations imposed by resolution and background. J Comput Assist Tomogr 1984;8:514–22.
[16] Herscovitch P, Auchus AP, Gado M, et al. Correction of positron emission tomography data for cerebral atrophy. J Cereb Blood Flow Metab 1986;6:120–4.
[17] Avril N, Bense S, Ziegler SI, et al. Breast imaging with fluorine-18-FDG PET: quantitative image analysis. J Nucl Med 1997;38:1186–91.
[18] Wahl LM, Asselin MC, Nahmias C. Regions of interest in the venous sinuses as input functions for quantitative PET. J Nucl Med 1999;40: 1666–75.
[19] Geworski L, Knoop BO, de Cabrejas ML, et al. Recovery correction for quantitation in emission tomography: a feasibility study. Eur J Nucl Med 2000;27:161–9.

[20] Menda Y, Bushnell DL, Madsen MT, et al. Evaluation of various corrections to the standardized uptake value for diagnosis of pulmonary malignancy. Nucl Med Commun 2001;22: 1077–81.
[21] Fleming JS, Bolt L, Stratford JS, et al. The specific uptake size index for quantifying radiopharmaceutical uptake. Phys Med Biol 2004;49: N227–34.
[22] Tossici-Bolt L, Hoffmann SMA, Kemp PM, et al. Quantification of [123I]FP-CIT SPECT brain images: an accurate technique for measurement of the specific binding ratio. Eur J Nucl Med Mol Imaging 2006;33:1491–9.
[23] Rousset O, Ma Y, Kamber M, et al. 3D simulations of radiotracer uptake in deep nuclei of human brain. Comput Med Imaging Graph 1993; 17:373–9.
[24] Rousset OG, Ma Y, Marenco S, et al. In vivo correction for partial volume effects in PET: accuracy and precision. In: Myers R, Cunningham V, Bailey DL, editors. Quantification of brain function using PET, vol. 1. San Diego (CA): Academic Press; 1996. p. 158–65.
[25] Rousset OG, Ma Y, Evans AC. Correction for partial volume effects in PET: principle and validation. J Nucl Med 1998;39:904–11.
[26] Du Y, Tsui BMW, Frey EC. Partial volume effect compensation for quantitative brain SPECT imaging. IEEE Trans Med Imaging 2005;24: 969–76.
[27] Du Y, Tsui BMW, Frey EC. Model-based compensation for quantitative 123I brain SPECT imaging. Phys Med Biol 2006;51:1269–82.
[28] Labbe C, Froment JC, Kennedy A, et al. Positron emission tomography metabolic data corrected for cortical atrophy using magnetic resonance imaging. Alzheimer Dis Assoc Disord 1996;10: 141–70.
[29] Aston JA, Cunningham VJ, Asselin MC, et al. Positron emission tomography partial volume correction: estimation and algorithms. J Cereb Blood Flow Metab 2002;22:1019–34.
[30] Barrett H, Wilson D, Tsui B. Noise properties of the EM algorithm: I. Theory. Phys Med Biol 1994;39:833–46.
[31] Qi J. A unified noise analysis for iterative image estimation. Phys Med Biol 2003;48:3505–19.
[32] Rahmim A, Cheng J-C, Sossi V. Improved noise propagation in statistical image reconstruction with resolution modeling. IEEE Nuclear Science Symposium Conference Record 2005;5:2576–8.
[33] Li Q, Asma E, Qi J, et al. Accurate estimation of the Fisher information matrix for the PET image reconstruction problem. IEEE Trans Med Imaging 2004;23:1057–64.
[34] Videen TO, Perlmutter JS, Mintun MA, et al. Regional correction of positron emission tomography data for the effects of cerebral atrophy. J Cereb Blood Flow Metab 1988;8:662–70.
[35] Muller-Gartner HW, Links JM, Prince JL, et al. Measurement of radiotracer concentration in brain gray matter using positron emission tomography: MRI-based correction for partial volume effects. J Cereb Blood Flow Metab 1992;12: 571–83.
[36] Rousset OG, Ma Y, Wong DF, et al. Pixel- versus region-based partial volume correction in PET. In: Carson R, Daube-Witherspoon ME, Herscovitch P, editors. Quantitative functional imaging with positron emission tomography. vol. 1. San Diego (CA): Academic Press; 1998. p. 67–75.
[37] Quarantelli M, Berkouk K, Prinster A, et al. Integrated software for the analysis of brain PET/ SPECT studies with partial-volume-effect correction. J Nucl Med 2004;45:192–201.
[38] Meltzer CC, Zubieta JK, Links JM, et al. MR-based correction of brain PET measurements for heterogeneous gray matter radioactivity distribution. J Cereb Blood Flow Metab 1996;16:650–8.
[39] Meltzer CC, Kinahan PE, Greer PJ, et al. Comparative evaluation of MR-based partial-volume correction schemes for PET. J Nucl Med 1999;40: 2053–65.
[40] Schafer RW, Mersereau RM, Richards MA. Constrained iterative restoration algorithms. Proc IEEE 1981;69:432–50.
[41] Carasso A. Linear and nonlinear image deblurring: a documented study. SIAM Journal on Numerical Analysis 1999;36:1659–89.
[42] Rudin L, Osher S, Fatemi E. Nonlinear total variation based noise removal algorithms. Physica D 1992;60:259–68.
[43] Teo B-K, Seo Y, Bacharach SL, et al. Partial-volume correction in PET: validation of an iterative postreconstruction method with phantom and patient data. J Nucl Med 2007;48:802–10.
[44] Boussion N, Hatt M, Lamare F, et al. A multiresolution image based approach for correction of partial volume effects in emission tomography. Phys Med Biol 2006;51:1857–76.
[45] Chiverton J, Wells K, Partridge M. A combined noise reduction and partial volume estimation method for image quantitation. Proceedings of the IEEE Nuclear Science Symposium and Medical Imaging Conference 2006;6:322–8.
[46] Qi J, Leahy RM. Iterative reconstruction techniques in emission computed tomography. Phys Med Biol 2006;51:R541–78.
[47] Reader A, Zaidi H. Advances in PET image reconstruction. PET Clinics 2007;2:173–90.
[48] Baete K, Nuyts J, Van Paesschen W, et al. Anatomical-based FDG-PET reconstruction for the detection of hypo-metabolic regions in epilepsy. IEEE Trans Med Imaging 2004;23:510–9.
[49] Huesman RH. A new fast algorithm for the evaluation of regions of interest and statistical uncertainty in computed tomography. Phys Med Biol 1984;29:543–52.
[50] Carson RE. A maximum likelihood method for region-of-interest evaluation in emission tomography. J Comput Assist Tomogr 1986;10: 654–63.

[51] Formiconi AR. Least squares algorithm for region of interest evaluation in emission tomography. IEEE Trans Med Imaging 1993;12:90–100.
[52] Vanzi E, De Cristofaro M, Ramat S, et al. A direct ROI quantification method for inherent PVE correction: accuracy assessment in striatal SPECT measurements. Eur J Nucl Med Mol Imaging 2007;34:1480–9.
[53] Rousset O, Zaidi H. Correction of partial volume effects in emission tomography. In: Zaidi H, editor. Quantitative analysis of nuclear medicine images. New York: Springer; 2006. p. 236–71.
[54] Reader AJ, Julyan PJ, Williams H, et al. EM algorithm system modeling by image-space techniques for PET reconstruction. IEEE Trans Nucl Sci 2003;50:1392–7.
[55] Panin VY, Kehren F, Michel C, et al. Fully 3-D PET reconstruction with system matrix derived from point source measurements. IEEE Trans Med Imaging 2006;25:907–21.
[56] Green PJ. Bayesian reconstructions from emission tomography data using a modified EM algorithm. IEEE Trans Med Imaging 1990;9: 84–93.
[57] Zhang Y, Fessler J, Clinthorne N, et al. Joint estimation for incorporating MRI anatomic images into SPECT reconstruction. In: Proceedings of the IEEE Nuclear Science Symposium and Medical Imaging Conference October 30–November 5, 1994, Norfolk, VA.
[58] Bowsher JE, Johnson VA, Turkington TG, et al. Bayesian reconstruction and use of anatomical a priori information for emission tomography. IEEE Trans Med Imaging 1996;15:673–86.
[59] Rangarajan A, Hsiao I-T, Gindi G. A Bayesian joint mixture framework for the integration of anatomical information in functional image reconstruction. J Mat Imag Vision 2000;12: 119–217.
[60] Muzic RF, Chen CH, Nelson AD. A method to correct for scatter, spillover, and partial volume effects in region of interest analysis in PET. IEEE Trans Med Imaging 1998;17:202–13.
[61] Chen CH, Muzic RF, Nelson AD, et al. Simultaneous recovery of size and radioactivity concentration of small spheroids with PET data. J Nucl Med 1999;40:118–30.
[62] Schoenahl F, Zaidi H. Towards optimal model-based partial volume effect correction in oncological PET imaging. Proceedings of the IEEE Nuclear Science Symposium and Medical Imaging Conference 2004;5:3177–81.
[63] Meltzer CC, Cantwell MN, Greer PJ, et al. Does cerebral blood flow decline in healthy aging? A PET study with partial-volume correction. J Nucl Med 2000;41:1842–8.
[64] Van Laere KJ, Dierckx RA. Brain perfusion SPECT: age- and sex-related effects correlated with voxel-based morphometric findings in healthy adults. Radiology 2001;221:810–7.
[65] Yanase D, Matsunari I, Yajima K, et al. Brain FDG PET study of normal aging in Japanese: effect of atrophy correction. Eur J Nucl Med Mol Imaging 2005;32:794–805.
[66] Ibanez V, Pietrini P, Alexander GE, et al. Regional glucose metabolic abnormalities are not the result of atrophy in Alzheimer's disease. Neurology 1998;50:1585–93.
[67] Knowlton RC, Laxer KD, Klein G, et al. In vivo hippocampal glucose metabolism in mesial temporal lobe epilepsy. Neurology 2001;57: 1184–90.
[68] Wong DF, Harris JC, Naidu S, et al. Dopamine transporters are markedly reduced in Lesch-Nyhan disease in vivo. Proc Natl Acad Sci U S A 1996;93:5539–43.
[69] Rousset OG, Deep P, Kuwabara H, et al. Effect of partial volume correction on estimates of the influx and cerebral metabolism of 6-[(18)F]fluoro-L-dopa studied with PET in normal control and Parkinson's disease subjects. Synapse 2000;37: 81–9.
[70] Henze E, Huang SC, Ratib O, et al. Measurements of regional tissue and blood-pool radiotracer concentrations from serial tomographic images of the heart. J Nucl Med 1983;24: 987–96.
[71] Herrero P, Markham J, Bergmann SR. Quantitation of myocardial blood flow with H2 15O and positron emission tomography: assessment and error analysis of a mathematical approach. J Comput Assist Tomogr 1989;13:862–73.
[72] Nuyts H, Maes A, Vrolix M, et al. Three-dimensional correction for spillover and recovery of myocardial PET images. J Nucl Med 1996;37: 767–74.
[73] Wassenaar RW, deKemp RA. Characterization of PET partial volume corrections for variable myocardial wall thicknesses. IEEE Trans Nucl Sci 2006;53:175–80.
[74] Vesselle H, Schmidt RA, Pugsley JM, et al. Lung cancer proliferation correlates with [F-18]Fluorodeoxyglucose uptake by positron emission tomography. Clin Cancer Res 2000; 6:3837–44.
[75] Vesselle H, Turcotte E, Wiens L, et al. Relationship between non-small cell lung cancer fluorodeoxyglucose uptake at positron emission tomography and surgical stage with relevance to patient prognosis. Clin Cancer Res 2004;10: 4709–16.
[76] Mankoff D, Dunnwald L, Gralow J, et al. Changes in blood flow and metabolism in locally advanced breast cancer treated with neoadjuvant chemotherapy. J Nucl Med 2003;44:1806–14.
[77] Soret M, Riddell C, Hapdey S, et al. Biases affecting the measurements of tumor-to-background activity ratio in PET. IEEE Trans Nucl Sci 2002;49:2112–8.
[78] Tatsumi M, Nakamoto Y, Traughber B, et al. Initial experience in small animal tumor imaging with a clinical positron emission tomography/computed tomography scanner using 2-[F-18] fluoro-2-deoxy-D-glucose. Cancer Res 2003;63: 6252–7.

[79] Basu S, Houseni M, Bural G, et al. Magnetic resonance imaging based bone marrow segmentation for quantitative calculation of pure red marrow metabolism using 2-deoxy-2-[F-18] fluoro-D: -glucose- positron emission tomography: a novel application with significant implications for combined structure-function approach. Mol Imaging Biol 2007;9:361–5.
[80] Pietrzyk U. Does PET/CT render software fusion obsolete? Nuklearmedizin 2005;44:S13–7.
[81] Frouin V, Comtat C, Reilhac A, et al. Correction of partial volume effect for PET striatal imaging: fast implementation and study of robustness. J Nucl Med 2002;43:1715–26.
[82] Slifstein M, Mawlawi O, Laruelle M. Partial volume effect correction: methodological consideration. In: Gjedde A, Hansen SB, Knudsen GM, et al, editors. Physiological imaging of the brain with PET. Volume 1. San Diego (CA): Academic Press; 2001. p. 67–75.
[83] Strul D, Bendriem B. Robustness of anatomically guided pixel-by-pixel algorithms for partial volume effect correction in positron emission tomography. J Cereb Blood Flow Metab 1999;19: 547–59.
[84] Zaidi H. Medical image segmentation: quo vadis. Comput Methods Programs Biomed 2006;84: 63–7.
[85] Suri JS, Singh S, Reden L. Computer vision and pattern recognition techniques for 2-D and 3-D MR cerebral cortical segmentation (part I): a state-of-the-art review. Pattern Anal Applicat 2002;5: 46–76.
[86] Zaidi H, Ruest T, Schoenahl F, et al. Comparative evaluation of statistical brain MR image segmentation algorithms and their impact on partial volume effect correction in PET. Neuroimage 2006;32:1591–607.
[87] Ashburner J, Friston KJ. Unified segmentation. Neuroimage 2005;26:839–51.
[88] Van Leemput K, Maes F, Vandermeulen D, et al. Automated model-based tissue classification of MR images of the brain. IEEE Trans Med Imaging 1999;18:897–908.
[89] Kovacevic N, Lobaugh NJ, Bronskill MJ, et al. A robust method for extraction and automatic segmentation of brain images. Neuroimage 2002;17:1087–100.
[90] Schlemmer H, Pichler BJ, Wienhard K, et al. Simultaneous MR/PET for brain imaging: first patient scans [abstract]. J Nucl Med 2007; 48:45.
[91] Zaidi H, Montandon M-L, Slosman DO. Magnetic resonance imaging-guided attenuation and scatter corrections in three-dimensional brain positron emission tomography. Med Phys 2003;30: 937–48.
[92] Evans A, Marrett S, Neelin P, et al. Anatomical mapping of functional activation in stereotactic coordinate space. Neuroimage 1992;1:43–53.